J Adv Ceram

Research Article

Simultaneous achievement of large strain, low hysteresis, and high-temperature stability in textured BT-based piezoelectric ceramics

Xiyue Zhang[1], Zhe Wang[1], Peng Li[1], Yingchun Liu[2], Juan Du[1], Jigong Hao[1,✉], Wei Li[1,✉], Jiwei Zhai[3,✉]

Cite this article: Zhang X, Wang Z, Li P, et al. *J Adv Ceram* 2025, **14**(2): 9221025. https://doi.org/10.26599/JAC.2024.9221025

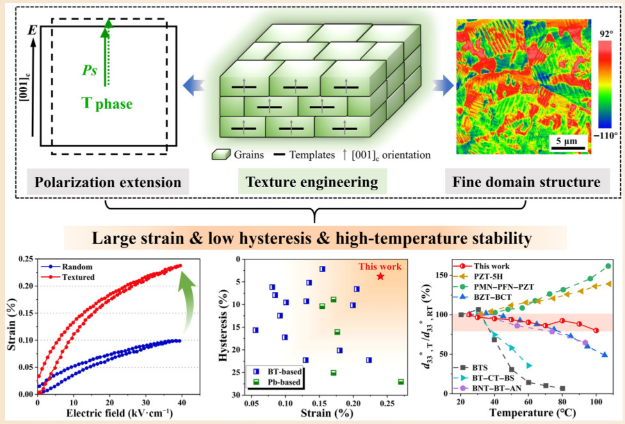

ABSTRACT: $BaTiO_3$ (BT)-based piezoceramics with large temperature-stable strains and low hysteresis are urgently needed for high-precision actuators because of increasing environmental problems. Here, tetragonal $[001]_c$-textured $(Ba_{0.98}Ca_{0.02})(Ti_{0.96}Sn_{0.04})O_3$ (BCTS) ceramics with a texture degree (F_{001}) of ~98% were obtained via the templated grain growth (TGG) method. A large maximum unipolar strain (S_{max}) of ~0.24% with a low strain hysteresis (H_s) of ~3.8% and an optimized piezoelectric strain coefficient (d_{33}*) of ~1124 pm·V^{-1} are simultaneously achieved in the textured BCTS ceramics. Moreover, the variation in the strain response is less than 20% from room temperature (RT) to 100 °C for the textured ceramics. The underlying mechanism for the optimized strain performance could be attributed to the synergetic effect of the polarization extension and a fine domain structure. This work provides new insight for achieving a balance of multiple strain properties (large strain, low hysteresis, and high-temperature stability) in BT-based ceramics, showing the widespread application prospects of lead-free ceramics in high-precision actuators.

KEYWORDS: textured ceramics; strain performance; hysteresis; temperature stability

1 Introduction

Piezoelectric actuators are integral electronic components in various fields, including fuel injectors, aerospace micro thrusters, and active vibration-damping systems [1,2]. Undoubtedly, large strain values and low hysteresis piezoelectric materials are essential for high-precision actuator applications [3]. Lead-based ceramics, such as $Pb(Zr,Ti)O_3$ (PZT)-based ceramics, are among the mainstream materials for most commercial piezoelectric actuators because of their superior comprehensive performance [4,5]. However, the presence of toxic lead increasingly causes damage to the natural environment and presents safety concerns. Recently, the development of lead-free piezoelectric ceramic actuators has become a significant area of research within the field of functional materials [6].

Among lead-free materials, $BaTiO_3$ (BT)-based ceramics are considered highly promising candidates for actuator applications owing to their exceptional piezoelectric properties. Many efforts have been made to increase the piezoelectric performance of BT-based ceramics by constructing phase boundaries among the rhombohedral (R), orthorhombic (O), tetragonal (T), and/or cubic (C) phases near room temperature (RT) through compositional modifications [7–11]. Excellent performance, including a large piezoelectric coefficient (d_{33}) of ~620 pC·N^{-1} and a high signal piezoelectric strain coefficient (d_{33}*) of 1140 pm·V^{-1}, was reported for $(Ba_{0.85}Ca_{0.15})(Ti_{0.90}Zr_{0.10})O_3$ piezoceramics [9], with the R–T–C tricritical point located near RT. Nevertheless, several serious problems in the application of high-precision actuators for BT-based ceramics need to be considered and addressed. BT-based ceramics exhibit obvious strain hysteresis (H_s) in electric-field-induced strain curves, which significantly impacts the precision of piezoelectric actuators and limits their application in precision control devices and systems [12,13]. In addition, virtually different from the morphotropic phase boundary of PZT-based materials, the polycrystalline phase transition of BT-based ceramics has the inherent disadvantage of

[1] School of Materials Science and Engineering, Laboratory of Sensitive Materials and Devices Shandong Department of Education, Liaocheng University, Liaocheng 252059, China. [2] Functional Materials and Acoustooptic Instruments Institute, Harbin Institute of Technology, Harbin 150080, China. [3] School of Materials Science and Engineering, Tongji University, Shanghai 201804, China.

✉ Corresponding authors. E-mail: J. Hao, haojigong@lcu.edu.cn; W. Li, liwei_727@163.com; J. Zhai, apzhai@tongji.edu.cn

Received: September 11, 2024; Revised: November 27, 2024; Accepted: December 28, 2024

poor temperature stability, which severely hinders industrial applications [7,8,13–15].

Currently, texture engineering with a crystallographic orientation, which can be achieved via the templated grain growth (TGG) method, effectively utilizes the intrinsic anisotropy of materials to improve their piezoelectric/strain properties [16–21]. Another important feature of textured ceramics is their low hysteresis. For example, $[001]_c$ textured $(Ba_{0.95}Ca_{0.05})(Ti_{0.96}Zr_{0.04})O_3$ ceramics have been developed by Liu [16]. The corresponding d_{33} and d_{33}* values exhibit peak values of approximately 780 pC·N^{-1} and 2950 pm·V^{-1}, respectively, whereas an ultralow H_s of 5.2% was obtained. The enhanced piezoelectric properties could be attributed to polarization rotation facilitated by the formation of 4R- and/or 4O-engineered multidomain structures in textured ceramics with an R or O phase poled along the $[001]_c$ [22,23]. The significantly reduced H_s is due to the stable domain structures, which could reduce the driving force for domain wall motion [24]. However, few BT-based piezoelectric ceramics with high strain and low hysteresis across a broad temperature range have been reported. Therefore, effectively reducing strain hysteresis and improving temperature stability while achieving high strain performance is an urgent task for BT-based piezoelectric ceramics.

Research conducted on various ceramic materials, including $Pb(Mg_{1/3}Nb_{2/3})O_3$–$PbTiO_3$-based ceramics [25], (Ba,Ca)(Zr,Ti)O_3-based ceramics [17], and $KNaNbO_3$-based ceramics [26], has demonstrated that the T phase is favorable for improving the temperature stability of these materials. For tetragonal textured ceramics, one domain variant with polar vectors along [001] will be promoted energetically by the poling field along the polar axis [001], which labels the "1T" engineered domain structure [27,28]. Ferroelectricity with the 1T single-domain state exhibits an enhanced piezoelectric performance along the $[001]_c$ polarity direction because of the polarization extension [17,26,29], whereby a lengthening of the polar vector, which results in lattice strain by poling along the polar vector [30,31]. Thus, we propose a strategy combining texture engineering and phase structure adjustment, expecting to achieve a large strain with low hysteresis and high-temperature stability in tetragonal BT-based textured ceramics.

In this work, we choose $(Ba_{0.98}Ca_{0.02})(Ti_{0.96}Sn_{0.04})O_3$ (BCTS) as the basis material owing to the dominant T phase in the O–T coexisting phase and its reasonable Curie temperature (T_c) [32]. Furthermore, textured ceramics are expected to display enhanced piezoelectric properties without affecting T_c of the material. Strong $[001]_c$-grain orientation textured $(Ba_{0.98}Ca_{0.02})(Ti_{0.96}Sn_{0.04})O_3$ ceramics, which are dominated by the T phase, were fabricated on 4.0 mol% $BaTiO_3$ templates via TGG technology. The effects of crystallographic orientation on the structure, dielectric properties, piezoelectric/strain performance, and domain morphology of BCTS ceramics were systematically explored. On the basis of the results of electrical and structural characterization, the potential sources of the superior strain performance of the BCTS textured ceramics are revealed. This research proposes textured BCTS ceramics with temperature-stable large strain and low hysteresis, which facilitates the use of lead-free piezoelectric ceramics in high-precision actuator applications.

2 Materials and methods

2.1 Experimental procedures

The textured $(Ba_{0.98}Ca_{0.02})(Ti_{0.96}Sn_{0.04})O_3$ ceramics were synthesized via the TGG method, as shown in Fig. S2 in the Electronic Supplementary Material (ESM). A mixture of $BaCO_3$, $CaCO_3$, TiO_2, and SnO_2 (Table S1 in the ESM) was ball-milled in ethanol solution at 250 r·min^{-1} for 24 h. Following the drying process, the dried powders were heated to 1200 °C at 3 °C·min^{-1} and held in air for 2 h. The calcined powders were ball milled again in ethanol solution at 250 r·min^{-1} for 64 h. The matrix powders were initially blended with 27 wt% solvents (ethanol and toluene), 16.7 wt% binders, 1.0 wt% plasticizers, 0.2 wt% dispersants, and 0.1 wt% defoamers via ball milling at 300 r·min^{-1} for 12 h to obtain a homogeneous, agglomerate-free slurry. Subsequently, 4.0 mol% BT templates were added to the slurries, which were then mixed by ball-milling at 250 r·min^{-1} for 0.5 h, forming a tape-casting slurry. The slurry was tape cast at a rate of 100 cm·min^{-1} through a doctor blade with a height of 150 μm. The dried green tapes were cut, stacked, and subsequently laminated at 65 °C, 12 MPa for 15 min. The green samples were heated to 600 °C at 1 °C·min^{-1} and held for 5 h to remove organics, and then subjected to cold isostatic pressing at 200 MPa for 30 s. Finally, the samples were sintered to 1450 °C at 3 °C·min^{-1} and held for 3–4 h in air. For comparison, random BCTS ceramics were synthesized using the same steps as above without the addition of BT templates.

2.2 Characterizations

The phase structures were examined via an X-ray diffractometer (XRD; SmartLab 9kW, Rigaku, Japan), and the pseudocubic $[001]_c$ texture degree was measured via the pseudocubic Lotgering factor (F_{001}) [33]. The microstructures were observed via a field-emission scanning electron microscope (FE-SEM; Merlin Compact, Carl Zeiss, Germany). The electron backscatter diffraction (EBSD) pole figures and inverse pole figures were acquired on an FE-SEM instrument equipped with an EBSD attachment (AZtec EBSD system, Oxford Instruments, UK). Raman spectra were determined via a laser microscopic confocal Raman spectrometer (MonoVista CRS+, Spectroscopy & Imaging, Germany). Dielectric analysis was conducted via an LCR meter (E4980A, Agilent, USA). Polarization–electric (P–E) field loops and strain–electric (S–E) field curves were obtained on a ferroelectric measuring instrument (TF Analyzer 2000, aixACCT, Germany) with a frequency of f = 10 Hz. The piezoelectric coefficient (d_{33}) was evaluated by a d_{33} meter (ZG-4, Institute of Acoustics, China), on which the piezoelectric voltage coefficient (g_{33}) was calculated. The planar electromechanical coupling factor (k_p) was measured by an impedance analyzer (4294A, Agilent, USA). The domain structures were analyzed via an atomic force microscope (AFM; FM-Nanoview, China).

3 Results and discussion

3.1 Structural properties

Figure 1(a) displays the XRD patterns of the random and textured BCTS ceramics. The two types of BCTS ceramics display a pure perovskite phase, in which the textured ceramics exhibit a markedly increased intensity of the $(00l)_c$ diffraction peaks. The texture degree (F_{001}) of the textured ceramics calculated via Eqs. (1)–(3):

$$F_{001} = \frac{P - P_0}{1 - P_0} \times 100\% \tag{1}$$

$$P = \frac{\sum I_{(001)}}{\sum I_{(hkl)}} \tag{2}$$

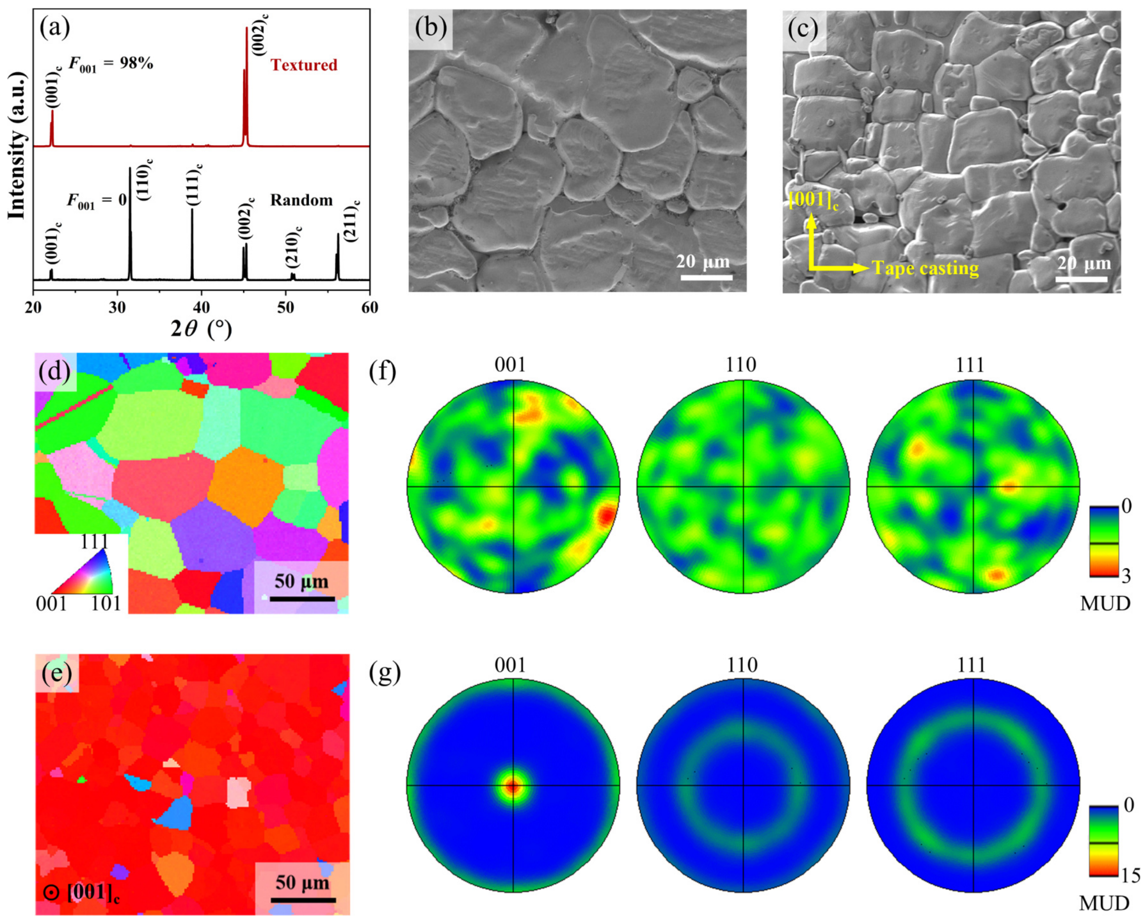

Fig. 1 (a) XRD patterns, (b, c) cross-sectional SEM images, and (d, e) inverse pole figure $[001]_c$ orientation maps for random and textured ceramics. (f, g) Pole figures corresponding to (d) and (e), respectively.

$$P_0 = \frac{\sum I_{0_{(00l)}}}{\sum I_{0_{(hkl)}}} \quad (3)$$

where I and I_0 represent the XRD peak intensities of the textured and random ceramics, respectively, while P and P_0 denote the pole densities of the $(001)_c$ plane in the textured and random ceramics, respectively. F_{001} is as high as 98%. This result indicates the presence of a pronounced $[001]_c$ orientation of the grains in the textured ceramics.

The cross-sectional SEM images of the random and textured BCTS ceramics are shown in Figs. 1(b) and 1(c), respectively. The textured ceramics show a “brick wall-like” grain morphology, which is arranged in a parallel orientation to the tape-casting direction (Fig. 1(c)). In contrast, the random ceramics display a uniform grain size distribution with randomly oriented grains (Fig. 1(b)). The average grain size of textured ceramics is approximately 20 μm, which is smaller than that of their random counterpart (35 μm) (Fig. S1 in the ESM). This difference can be attributed to the constrained sintering induced by the templates, which may have prevented grain growth during the final densification stage [34]. EBSD technology was used to investigate the degree of texture [35]. A comparison of the inverse pole figure maps for the random (Fig. 1(d)) and textured (Fig. 1(e)) ceramics reveals a pronounced $[001]_c$-crystal orientation of the textured ceramics. This result is further demonstrated by the pole figures shown in Fig. 1(g), which indicates that the pole density distribution is predominantly concentrated at the center of the $(001)_c$ pole figure. This suggests that the majority of the polycrystalline planes in the textured ceramics are parallel to $(001)_c$. In contrast, the pole density distributions for the $(001)_c$, $(110)_c$, and $(111)_c$ pole figures of the nontextured counterparts (Fig. 1(f)) are uniform across the spherical surface, indicating a completely random orientation [36].

Figure 2(a) displays the Raman spectra of the random and textured ceramics. The notable spectral dip near 140 cm^{-1} is attributed to the A-site coupling pattern [37], potentially resulting from phonon damping associated with the O phase structure [15]. The modes at approximately 301 cm^{-1} are typically regarded as an indication of the T phase [37]. These findings indicate the presence of an O–T phase mixture in these samples. Rietveld refinement was used to explore the detailed phase structure analysis further, as illustrated in Figs. 2(b) and 2(c). All of the samples were ground into fine powders for good-quality data and more reliable refinement results. The low reliability factors, including the weighted profile R-factor (R_{wp}) ≤ 7.24%, the profile R-factor (R_p) ≤ 5.61%, and the chi-square (χ^2) ≤ 1.23, prove the reliability of the Rietveld refinement results. All the BCTS ceramic samples exhibit the coexistence of O and T phases. The contents of the O and T phases in the random ceramics are 20.3% and 79.7%, respectively, whereas the T phase amount increases to 86.5% for the textured ceramics. Combined with the XRD data (splitting of the $(002)_c$ peak in Fig. 1(a)) and Rietveld refinement results, the textured BCTS ceramics are primarily T phase structures. The atomic parameters of the random and textured ceramics provided by Rietveld refinements (Tables S2 and S3 in the ESM) confirm that the atomic occupancy content of the BCTS is in accordance with the designed composition. To further prove the reliability of the results, the elemental atomic percentage obtained via EDS mapping is provided in Table S4 in the ESM, which is nearly the same as the stoichiometric composition of $(Ba_{0.98}Ca_{0.02})(Ti_{0.96}Sn_{0.04})O_3$.

3.2 Significantly enhanced strain properties

Figure 3(a) displays the temperature-dependent permittivity curves of the random and textured BCTS ceramics at various frequencies, including 1 kHz, 10 kHz, 100 kHz, and 1 MHz. Two pronounced dielectric anomalies are observed in both samples, corresponding to the O–T and T–C phase transitions. The shift of the T_c and T_{O-T} peaks to low temperatures in textured ceramics is related to the lattice distortion caused by interfacial stress between the matrix grains and BT templates, which leads to a variety of phase transition temperatures [24]. The maximum dielectric permittivity (ε_m) at T_c decreases significantly following the introduction of BT templates, which could be attributed to two dominant factors. One such factor is the elastoelectric composite effect, which is caused by the interfacial stresses between oriented grains and BT templates [34]. The other factor is related to the dielectric anisotropy. In accordance with engineering domain theory, the 1T engineering domain structure with the lowest dielectric properties is formed by polarization along the $[001]_c$ direction [38]. Figs. 3(b) and 3(c) show the typical well-saturated *P–E* hysteresis curves of all the samples measured at different maximum electrical fields (E_{max}), revealing their robust ferroelectricity. The two *P–E* curves at ±40 kV·cm^{-1} are compared in Fig. 3(d). The remanent polarization (P_r) of the textured ceramics (10.4 μC·cm^{-2}) is greater than that of the random ceramics (9.1 μC·cm^{-2}), with minimal impact on the coercive field (E_c). Theoretically, the polarization of textured ceramics with the

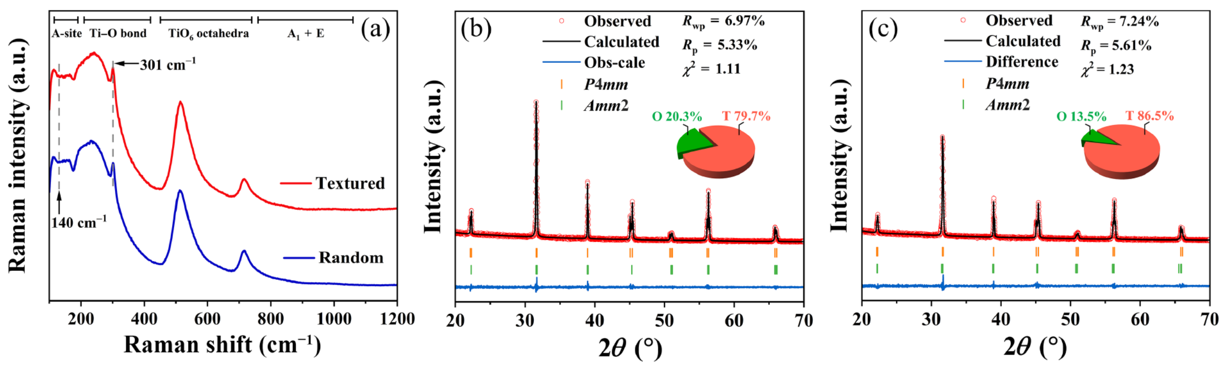

Fig. 2 (a) Raman spectra of random and textured ceramics. Rietveld refinement of XRD pattern of as-ground powders for (b) random and (c) textured ceramics.

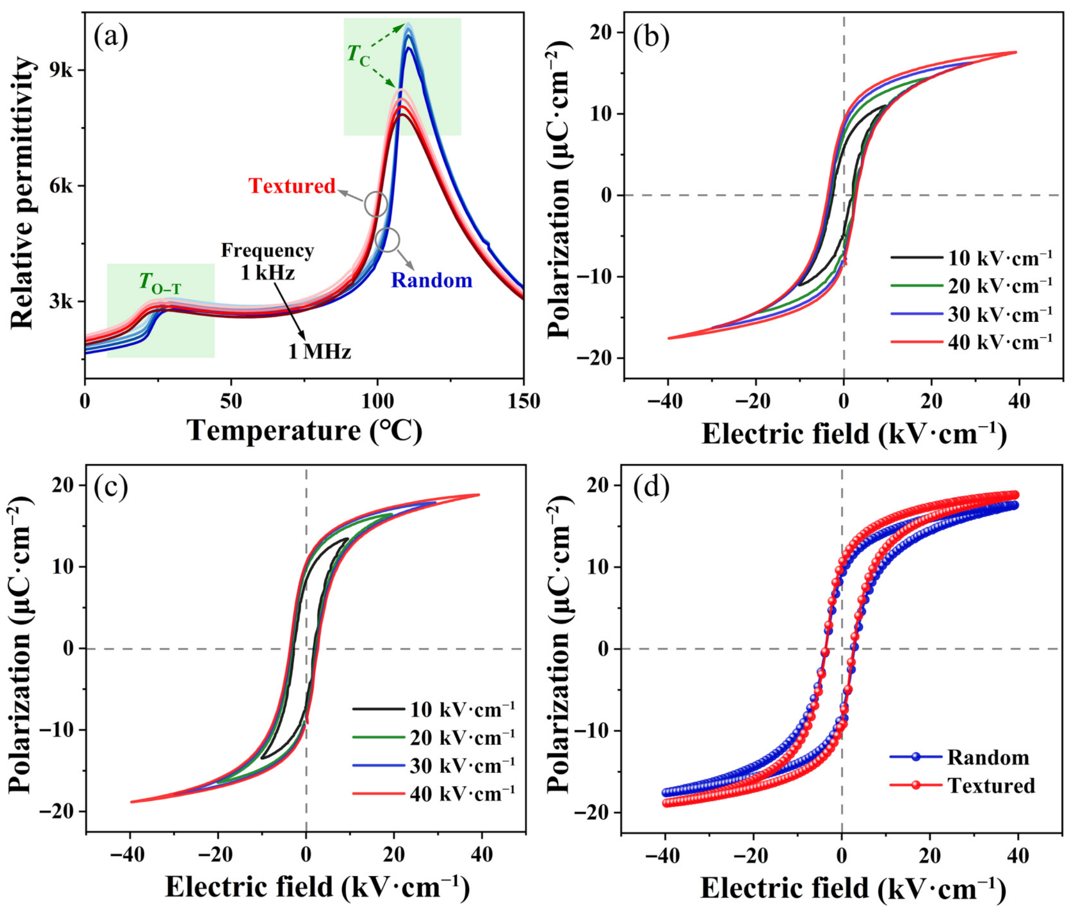

Fig. 3 (a) Permittivity–temperature curves at different frequencies. *P–E* loops of (b) random and (c) textured ceramics. (d) Comparison of the two *P–E* loops at ±40 kV·cm^{-1}.

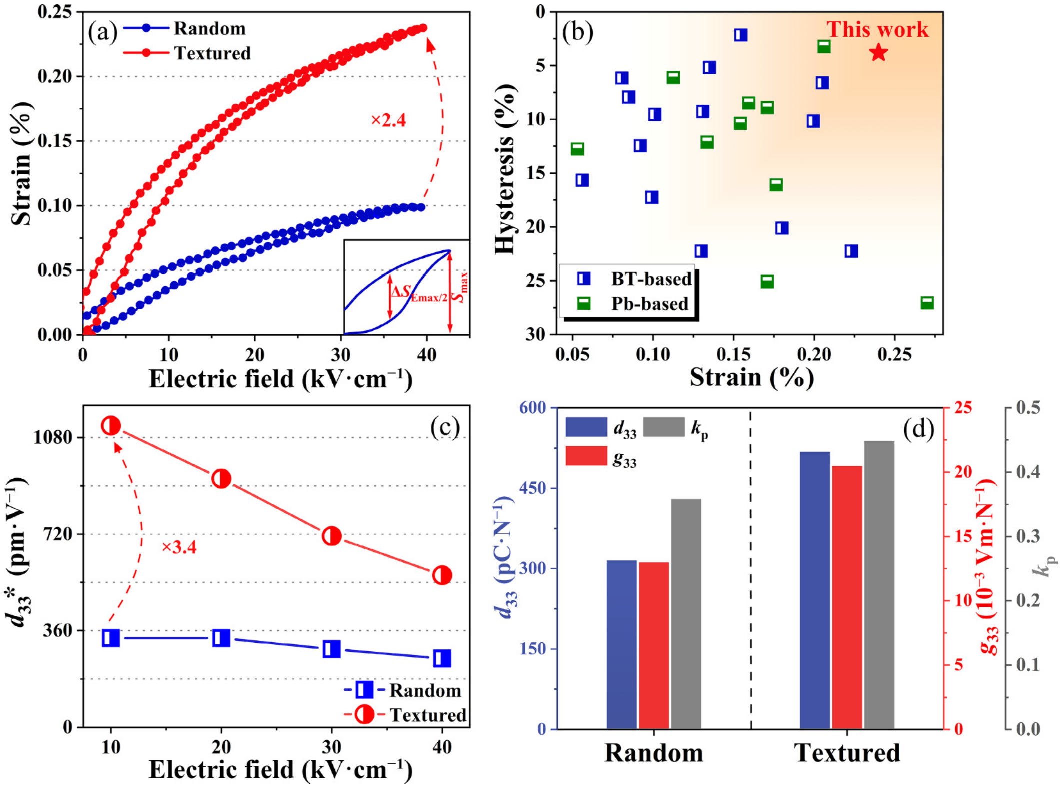

Fig. 4 (a) Unipolar *S*–*E* curves of two types of BCTS ceramics measured at 40 kV·cm⁻¹. (b) Comparison of S_{max} and corresponding H_s (= $\Delta S_{Emax/2}/S_{max}$) between this work (BCTS textured ceramics) and several typical lead-based ceramics and BT-based representative ceramics. (c) Variations in d_{33}* values with increasing electric field; (d) d_{33}, g_{33}, and k_p values of the random and textured BCTS ceramics.

T phase is stronger in the spontaneous polarization direction $[001]_c$ than in the nonpolar directions $[011]_c$ and $[111]_c$ [39].

Figure 4(a) displays the unipolar *S*–*E* curves measured at 40 kV·cm⁻¹. The textured ceramics exhibit a superior strain of 0.24%, which is approximately 2.4 times greater than that of the random ceramics. More importantly, the H_s of textured ceramics has been demonstrated to be 3.8% lower than that of random ceramics (10.10%), which is beneficial for improving the working accuracy and sensitivity of piezoelectric actuators. A comparison of the maximum unipolar strain (S_{max}) and H_s values obtained in this work with those of several typical lead-based ceramics [40–48] and BT-based representative ceramics [13,49–56] is displayed in Fig. 4(b). The textured BCTS ceramics investigated here exhibit a superior strain value and remarkably low hysteresis, outperforming the majority of previous studies. Fig. 4(c) compares the d_{33}* values of the random and textured ceramics with increasing electric field. The random ceramics exhibit d_{33}* of ~332 pm·V⁻¹ at 10 kV·cm⁻¹. In contrast, d_{33}* of the textured ceramics significantly increased to ~1124 pm·V⁻¹, which is almost 3.4 times that of the former. Fig. 4(d) shows the electromechanical-related performance, revealing the advantage of texture engineering in enhancing the piezoelectric performance of BCTS ceramics. The textured BCTS ceramics exhibit an enhanced d_{33} of ~520 pC·N⁻¹ and a large g_{33} of ~20.6×10⁻³ Vm·N⁻¹, which are nearly 1.6 times greater than those of their random counterparts (d_{33} of ~317 pC·N⁻¹, g_{33} of ~13.1 Vm·N⁻¹). The enhanced piezoelectric performance of textured BCTS ceramics is likely associated with the ease of domain reversal and mobility [57]. In addition, the textured ceramics present a k_p value of ~0.45.

3.3 Temperature stability of strain performance

To analyze the temperature stability of the strain performance, Figs. 5(a) and 5(b) show the temperature-dependent unipolar *S*–*E* loops of the two types of BCTS ceramics. Both the random and textured ceramics exhibit optimized temperature stability, with strain variations of 15% and 20%, respectively, between RT and 100 °C. The strain value of the textured ceramics is approximately twice as high as that of the random ceramics from RT to 100 °C (Fig. 5(c)), further demonstrating the advantages of textured BCTS ceramics in actuator applications. The T_{O-T} peak of the textured BCTS ceramics is at approximately 23 °C, which provides a wide stability range of the T phase below T_c and avoids the influence of the O–T phase transition on the strain properties above RT. The strain response is compared to that of several well-known piezoelectric ceramics in Fig. 5(d), which presents d_{33}*$_{,T}$/d_{33}*, and RT as a function of temperature. Compared with several representative piezoceramics, textured BCTS ceramics show superior temperature stability, including commercial PZT-5H [7,14,58–61]. Thus, introducing the $[001]_c$ texture to BCTS ceramics not only retains the exceptional temperature stability of the random ceramics from RT to 100 °C but also results in significantly increased strain values across the entire temperature range.

3.4 Mechanism responsible for high strain properties

The mechanisms by which crystallographic orientation enhances the strain response are graphically shown in Fig. 6. The high strain observed in ferroelectrics is primarily attributed to the combination of intrinsic lattice strain and extrinsic non-180° domain switching. The latter could lead to a large hysteresis [62]. For tetragonal BCTS textured ceramics, there are six equivalent spontaneous polarization directions of <001>, as shown in Fig. 6(a). After poling along the $[001]_c$ direction (above E_c), some of the polar vectors could align along the $[001]_c$ direction (Fig. 6(b)), i.e., 90° domain switching along the direction of $[001]_c$, forming a 1T single-domain state [27]. Upon further application of the electric

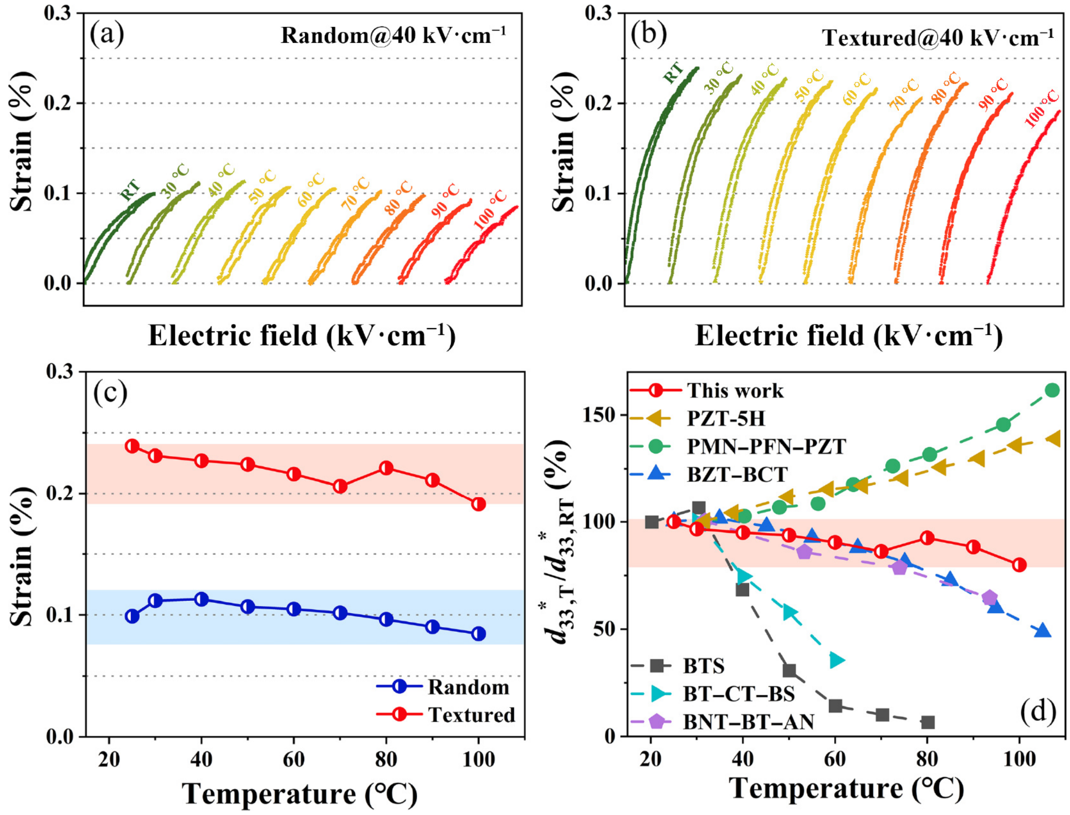

Fig. 5 (a, b) Unipolar *S*–*E* curves from RT to 100 °C, (c) unipolar strain variation as a function of temperature for random and textured ceramics. (d) Comparison of temperature dependence of normalized d_{33}* for textured BCTS ceramics in this work with those of other piezoceramics.

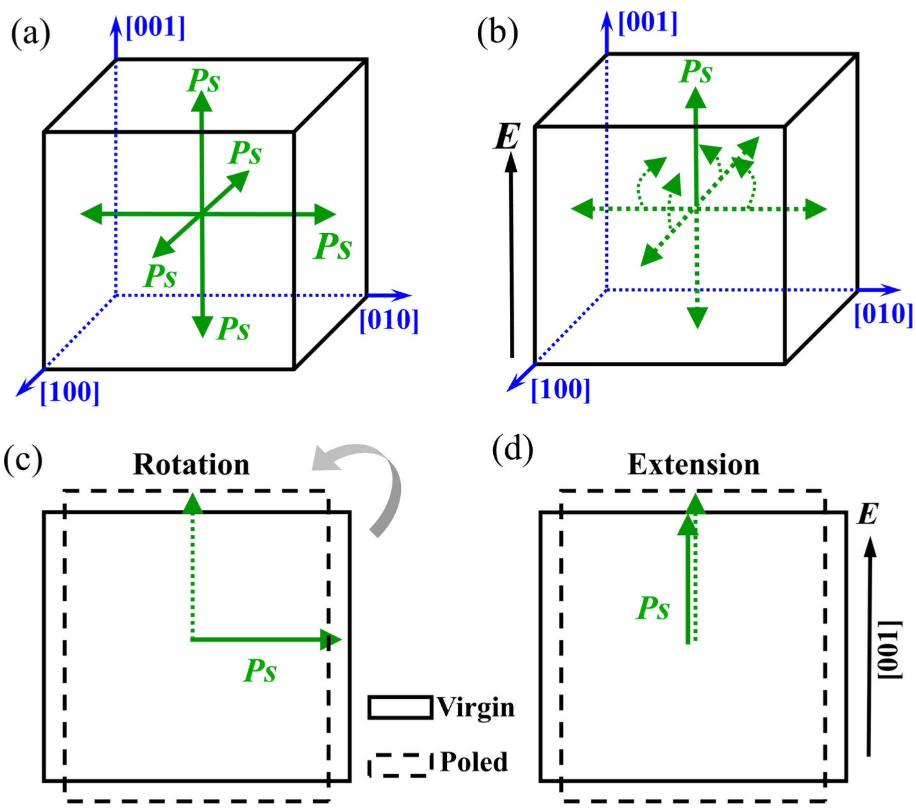

Fig. 6 Schematic diagrams of (a) domain-engineered configurations of tetragonal perovskite phase. (b) Rotation process of spontaneous polarization under an electric field. (c) Polarization rotation and (d) polarization extension.

field, the strain is derived mainly from the longitudinal lattice strain caused by polar vector elongation (polarization extension) (Fig. 6(d)) [30,31] rather than the rotation of the polar vector (polarization rotation) (Fig. 6(c)) [63]. This accounts for the low hysteresis strain characteristics in the textured ceramics at 40 kV·cm^{-1}. Thus, the increased intrinsic contribution caused by polarization extension is the underlying physical mechanism behind the coexistence of high strain and low hysteresis in textured BCTS ceramics.

3.5 Local domain structures

In addition to the intrinsic contribution (polarization extension), domain morphology also represents an effective method for enhancing electrical properties [64]. To reveal the effect of domain structures on the strain enhancement of textured ceramics, piezoresponse force microscope (PFM) measurements were performed on the BCTS ceramics, as presented in Fig. 7. Both types of ceramics are dominated by "stripe-like" domain structures (Figs. 7(a) and 7(b)), which are marked by white rectangles. The textured ceramics exhibit a much more ordered and uniform morphology, which could be related to the preferred orientation of the grains, facilitating coherent domain switching [17]. In particular, the average domain sizes measured by line scanning (Fig. 7(c)) differ substantially between the random and textured ceramics, e.g., 0.61 and 0.28 μm, respectively. The domains are formed to minimize the elastic energy [65]. The elastic energy of textured ceramics can be perturbed by the difference in size between the BT template and matrix grains, which leads to a finer domain structure in textured ceramics [66]. The domain size is related to the grain size effect [67], which decreases with decreasing grain size. Thus, the significantly decreased domain size of the textured ceramics is possibly caused by the reduced grain size (Figs. 1(b) and 1(c)). The smaller domains of the textured ceramics exhibit a higher density of domain walls. The classical domain theory, where D is the domain size, and E_{DW} is the domain wall energy, indicates that the domain size is proportional to the square root of the domain wall energy (Eq. (4)):

$$D \propto \sqrt{E_{DW}} \tag{4}$$

The formation of smaller domains is due to the lower domain wall energy [68], which can enhance piezoelectric performance by facilitating domain wall motion and coherent domain switching. Therefore, the enhanced strain response in the BCTS textured ceramics arises from a combination of the polarization extension (intrinsic contribution) and the fine domain structure (extrinsic contribution).

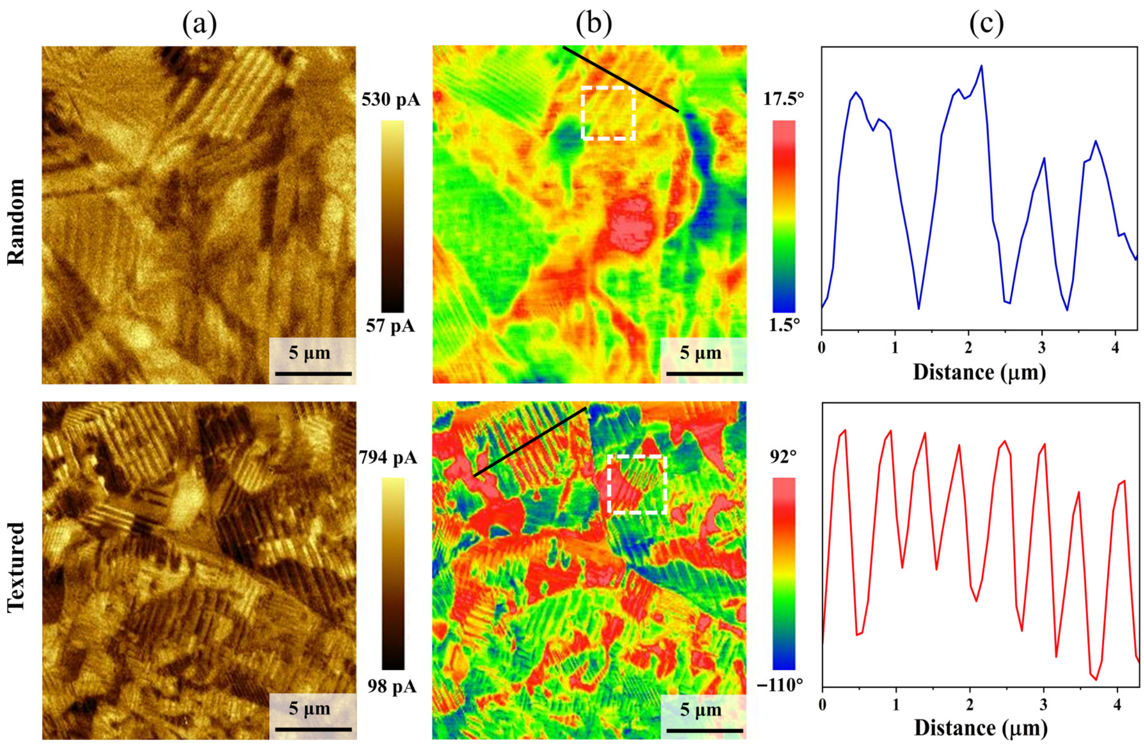

Fig. 7 (a) Out-of-plane PFM amplitude, (b) phase images, and (c) phase value variations along marked lines of the random and textured BCTS ceramics in phase images.

4 Conclusions

In summary, tetragonal [001]$_c$-oriented textured $(Ba_{0.98}Ca_{0.02})(Ti_{0.96}Sn_{0.04})O_3$ ceramics with BT templates were successfully fabricated via the TGG technique. A comprehensive investigation has been conducted on the structures, dielectric and piezoelectric performance, electromechanical coupling properties, strain response, and domain morphology of textured BCTS ceramics. As a result, high strain properties ($S_{max} \approx 0.24\%$, $H_s \approx 3.8\%$) and high piezoelectric performance ($d_{33} \approx 520$ pC·N^{-1}, $d_{33}^* \approx 1124$ pm·V^{-1}) were exhibited in the textured BCTS ceramics. Additionally, good temperature stability was achieved, in which the unipolar strain value varied less than 20% from RT to 100°C. The effects of the polarization extension mechanism and the fine-domain structure (~0.28 μm in domain size) of tetragonal textured ceramics on the strain response were discussed. The as-prepared BCTS textured ceramics, which exhibit high strain, ultralow hysteresis, and high-temperature stability, are promising lead-free candidates for the application of high-precision displacement actuators.

Acknowledgements

This work was supported by the National Natural Science

Foundation of China (No. 52102132), the Natural Science Foundation of Shandong Province of China (Nos. ZR2024ME201 and ZR2021ME085), the Guangdong Provincial Key Laboratory of Electronic Functional Materials and Devices (No. EFMD2023001M), and the Natural Science Foundation of Heilongjiang Province (No. LH2022E049).

Declaration of competing interest

The authors have no competing interests to declare that are relevant to the content of this article.

Electronic Supplementary Material

Supplementary material is available in the online version of this article at https://doi.org/10.26599/JAC.2024.9221025.

References

[1] Fan PY, Liu K, Ma WG, *et al.* Progress and perspective of high strain NBT-based lead-free piezoceramics and multilayer actuators. *J Materiomics* 2021, **7**: 508–544.

[2] Shu LL, Liang RH, Rao ZG, *et al.* Flexoelectric materials and their related applications: A focused review. *J Adv Ceram* 2019, **8**: 153–173.

[3] Yin J, Liu G, Zhao CL, *et al.* Perovskite $Na_{0.5}Bi_{0.5}TiO_3$: A potential family of peculiar lead-free electrostrictors. *J Mater Chem A* 2019, **7**: 13658–13670.

[4] Wang JJ, Wang SH, Li X, *et al.* High piezoelectricity and low strain hysteresis in PMN–PT-based piezoelectric ceramics. *J Adv Ceram* 2023, **12**: 792–802.

[5] Chen Y, Li LF, Zhou Z, *et al.* La_2O_3-modified $BiYbO_3$–Pb(Zr,Ti)O_3 ternary piezoelectric ceramics with enhanced electrical properties and thermal depolarization temperature. *J Adv Ceram* 2023, **12**: 1593–1611.

[6] Chen L, Yang YR, Meng XK. Giant electric-field-induced strain in lead-free piezoelectric materials. *Sci Rep* 2016, **6**: 25346.

[7] Wang DW, Fan ZM, Rao GH, *et al.* Ultrahigh piezoelectricity in lead-free piezoceramics by synergistic design. *Nano Energy* 2020, **76**: 104944.

[8] Fu J, Xie AW, Li TY, *et al.* Ultrahigh piezoelectricity in (Ba,Ca)(Ti,Sn)O_3 lead-free compounds with enormous domain wall contribution. *Acta Mater* 2022, **230**: 117862.

[9] Liu WF, Ren XB. Large piezoelectric effect in Pb-free ceramics. *Phys Rev Lett* 2009, **103**: 257602.

[10] Wang XJ, Huan Y, Zhu YX, *et al.* Defect engineering of BCZT-based piezoelectric ceramics with high piezoelectric properties. *J Adv Ceram* 2022, **11**: 184–195.

[11] Hayati R, Bahrevar MA, Ganjkhanlou Y, *et al.* Electromechanical properties of Ce-doped $(Ba_{0.85}Ca_{0.15})(Zr_{0.1}Ti_{0.9})O_3$ lead-free piezoceramics. *J Adv Ceram* 2019, **8**: 186–195.

[12] Ahn CW, Choi G, Kim IW, *et al.* Forced electrostriction by constraining polarization switching enhances the electromechanical strain properties of incipient piezoceramics. *NPG Asia Mater* 2017, **9**: 346.

[13] Jin L, Huo RJ, Guo RP, *et al.* Diffuse phase transitions and giant electrostrictive coefficients in lead-free Fe^{3+}-doped $0.5Ba(Zr_{0.2}Ti_{0.8})O_3$–$0.5(Ba_{0.7}Ca_{0.3})TiO_3$ ferroelectric ceramics. *ACS Appl Mater Inter* 2016, **8**: 31109–31119.

[14] Zhu LF, Zhang BP, Zhao L, *et al.* High piezoelectricity of $BaTiO_3$–$CaTiO_3$–$BaSnO_3$ lead-free ceramics. *J Mater Chem C* 2014, **2**: 4764–4771.

[15] Chaiyo N, Cann DP, Vittayakorn N. Lead-free (Ba,Ca)(Ti,Zr)O_3 ceramics within the polymorphic phase region exhibiting large, fatigue-free piezoelectric strains. *Mater Design* 2017, **133**: 109–121.

[16] Liu YC, Zhang HJ, Shi WM, *et al.* Ultrahigh strain in textured BCZT-based lead-free ceramics with CuO sintering agent. *J Mater Sci Technol* 2022, **117**: 207–214.

[17] Kou QW, Yang B, Sun Y, *et al.* Tetragonal (Ba,Ca)(Zr,Ti)O_3 textured ceramics with enhanced piezoelectric response and superior temperature stability. *J Materiomics* 2022, **8**: 366–374.

[18] Kou QW, Yang B, Lei HB, *et al.* Lead-free textured ceramics with ultrahigh piezoelectric properties by synergistic design. *ACS Appl Mater Inter* 2023, **15**: 37706–37716.

[19] Zhang Z, Duan XM, Tian Z, *et al.* Texture and anisotropy of hot-pressed h-BN matrix composite ceramics with *in situ* formed YAG. *J Adv Ceram* 2022, **11**: 532–544.

[20] Zhou XF, Yang HP, Xue GL, *et al.* Optimized strain performance in-textured $Bi_{0.5}Na_{0.5}TiO_3$-based ceramics with ergodic relaxor state and core–shell microstructure. *J Adv Ceram* 2022, **11**: 1542–1558.

[21] Lai LX, Zhao ZH, Tian S, *et al.* Ultrahigh electrostrain with excellent fatigue resistance in textured Nb^{5+}-doped $(Bi_{0.5}Na_{0.5})TiO_3$-based piezoceramics. *J Adv Ceram* 2023, **12**: 487–497.

[22] Liu YC, Chang YF, Sun EW, *et al.* Significantly enhanced energy-harvesting performance and superior fatigue-resistant behavior in $[001]_c$-textured $BaTiO_3$-based lead-free piezoceramics. *ACS Appl Mater Inter* 2018, **10**: 31488–31497.

[23] Sun Y, Chang YF, Wu J, *et al.* Ultrahigh energy harvesting properties in textured lead-free piezoelectric composites. *J Mater Chem A* 2019, **7**: 3603–3611.

[24] Liu YC, Chang YF, Li F, *et al.* Exceptionally high piezoelectric coefficient and low strain hysteresis in grain-oriented (Ba,Ca)(Ti,Zr)O_3 through integrating crystallographic texture and domain engineering. *ACS Appl Mater Inter* 2017, **9**: 29863–29871.

[25] Yan YK, Yang LJ, Zhou Y, *et al.* Enhanced temperature stability in <111> textured tetragonal $Pb(Mg_{1/3}Nb_{2/3})O_3$–$PbTiO_3$ piezoelectric ceramics. *J Appl Phys* 2015, **118**: 104101.

[26] Xue HY, Zheng T, Wu JG. Insights into the correlation between tetragonal phase and temperature stability of potassium sodium niobate based ceramics from domain behaviors. *Adv Electron Mater* 2022, **8**: 2100257.

[27] Ge WW, Luo CT, Zhang QH, *et al.* Ultrahigh electromechanical response in $(1-x)(Na_{0.5}Bi_{0.5})TiO_{3-x}BaTiO_3$ single-crystals via polarization extension. *J Appl Phys* 2012, **111**: 093508.

[28] Zhang SJ, Li F. High performance ferroelectric relaxor-$PbTiO_3$ single crystals: Status and perspective. *J Appl Phys* 2012, **111**: 031301.

[29] Yin J, Shi XM, Tao H, *et al.* Deciphering the atomic-scale structural origin for large dynamic electromechanical response in lead-free $Bi_{0.5}Na_{0.5}TiO_3$-based relaxor ferroelectrics. *Nat Commun* 2022, **13**: 6333.

[30] Fu J, Zuo RZ, Xu YD, *et al.* Investigations of domain switching and lattice strains in (Na,K)NbO_3-based lead-free ceramics across orthorhombic-tetragonal phase boundary. *J Eur Ceram Soc* 2017, **37**: 975–983.

[31] Karthik T, Asthana S. Polarization extension mechanism revealed through dynamic ferroelectric hysteresis and electric field driven structural distortions in lead free $Na_{0.5}Bi_{0.5}TiO_3$ ceramic. *J Phys D Appl Phys* 2017, **50**: 385601.

[32] Li W, Xu ZJ, Chu RQ, *et al.* Large piezoelectric coefficient in $(Ba_{1-x}Ca_x)(Ti_{0.96}Sn_{0.04})O_3$ lead-free ceramics. *J Am Ceram Soc* 2011, **94**: 4131–4133.

[33] Yamada T. Electromechanical properties of oxygen-octahedra ferroelectric crystals. *J Appl Phys* 1972, **43**: 328–338.

[34] Messing GL, Trolier-McKinstry S, Sabolsky EM, *et al.* Templated grain growth of textured piezoelectric ceramics. *Crit Rev Solid State Mater Sci* 2004, **29**: 45–96

[35] Yan YK, Zhou Y, Priya S. Enhanced electromechanical coupling in $Pb(Mg_{1/3}Nb_{2/3})O_3$–$PbTiO_3$ $\langle 001\rangle_c$ radially textured cylinders. *Appl Phys Lett* 2014, **104**: 012910.

[36] Shin HJ, An JK, Park SH, *et al.* The effect of texture on ridging of ferritic stainless steel. *Acta Mater* 2003, **51**: 4693–4706.

[37] Fleury PA, Lazay PD. Acoustic—Soft-optic mode interactions in ferroelectric $BaTiO_3$. *Phys Rev Lett* 1971, **26**: 1331–1334.

[38] Sun EW, Cao WW. Relaxor-based ferroelectric single crystals: Growth, domain engineering, characterization and applications. *Prog Mater Sci* 2014, **65**: 124–210.

[39] Zhao XY, Wang J, Peng Z, *et al.* Triple-like hysteresis loop and microdomain–macrodomain transformation in the relaxor-based $0.76Pb(Mg_{1/3}Nb_{2/3})O_3$–$0.24PbTiO_3$ single crystal. *Mater Res Bull* 2004, **39**: 223–230.

[40] Yan YK, Cho KH, Priya S. Templated grain growth of <001>-textured 0.675Pb($Mg_{1/3}Nb_{2/3}$)O_3–0.325PbTiO_3 piezoelectric ceramics for magnetic field sensors. *J Am Ceram Soc* 2011, **94**: 1784–1793.

[41] Zeng JT, Zhao KY, Ruan W, *et al.* Contribution to the large and stable electric field induced strain for textured Pb($Mg_{1/3}Nb_{2/3}$)$_{0.675}$ $Ti_{0.325}O_3$ ceramics. *Appl Phys Lett* 2016, **109**: 052905.

[42] Hao MM, Fan GF, Cai W, *et al.* A quasi-linear piezoelectric strain behavior of [001] textured rhombohedral PMN–24%PT ceramic. *J Am Ceram Soc* 2020, **103**: 6226–6236.

[43] Guo QH, Meng XY, Li F, *et al.* Temperature-insensitive PMN–PZ–PT ferroelectric ceramics for actuator applications. *Acta Mater* 2021, **211**: 116871.

[44] Dong SS, Guo FF, Zhou HQ, *et al.* Phase structures and electrical properties of Sm doped PSN–PMN–PT ceramics. *J Alloys Compd* 2021, **881**: 160621.

[45] Kumar A, Kim SH, Peddigari M, *et al.* High energy storage properties and electrical field stability of energy efficiency of ($Pb_{0.89}La_{0.11}$)($Zr_{0.70}Ti_{0.30}$)$_{0.9725}O_3$ relaxor ferroelectric ceramics. *Electron Mater Lett* 2019, **15**: 323–330.

[46] Yang Y, Liu C, Ji YC, *et al.* Designed morphotropic relaxor boundary ceramic exhibiting large electrostrain and negligible hysteresis. *Acta Mater* 2021, **208**: 116720.

[47] Yao RH, Liu YF, Lyu CG, *et al.* Impact of Ni dopant on structure and electrical properties of PMN–0.1PT ceramics. *J Mater Sci-Mater El* 2017, **28**: 7525–7531.

[48] Jin L, Luo WT, Jing RY, *et al.* High dielectric permittivity and electrostrictive strain in a wide temperature range in relaxor ferroelectric $(1-x)$[Pb($Mg_{1/3}Nb_{2/3}$)O_3–PbTiO_3]–xBa($Zn_{1/3}Nb_{2/3}$)O_3 solid solutions. *Ceram Int* 2019, **45**: 5518–5524.

[49] Li F, Jin L, Guo RP. High electrostrictive coefficient Q_{33} in lead-free Ba($Zr_{0.2}Ti_{0.8}$)O_3–$_x$($Ba_{0.7}Ca_{0.3}$)TiO_3 piezoelectric ceramics. *Appl Phys Lett* 2014, **105**: 232903.

[50] Huang YL, Zhao CL, Yin J, *et al.* Giant electrostrictive effect in lead-free barium titanate-based ceramics via A-site ion-pairs engineering. *J Mater Chem A* 2019, **7**: 17366–17375.

[51] Jin L, Luo WT, Hou L, *et al.* High electric field-induced strain with ultra-low hysteresis and giant electrostrictive coefficient in barium strontium titanate lead-free ferroelectrics. *J Eur Ceram Soc* 2019, **39**: 295–304.

[52] Jin L, Luo WT, Wang L, *et al.* High thermal stability of electric field-induced strain in $(1-x)$($Bi_{0.5}Na_{0.5}$)TiO_3–$_x$$Ba_{0.85}Ca_{0.15}Ti_{0.9}Zr_{0.1}O_3$ lead-free ferroelectrics. *J Eur Ceram Soc* 2019, **39**: 277–286.

[53] Jin L, Qiao J, Hou L, *et al.* A strategy for obtaining high electrostrictive properties and its application in barium stannate titanate lead-free ferroelectrics. *Ceram Int* 2018, **44**: 21816–21824.

[54] Wu WJ, Ma J, Wang NN, *et al.* Electrical properties, strain stability and electrostrictive behavior in 0.5Ba$Zr_{0.2}Ti_{0.8}O_3$–$(0.5-x)$$Ba_0$.7$Ca_{0.3}$ TiO_3–$_x$$Ba_{0.7}Sr_{0.3}TiO_3$ lead-free ceramics. *J Alloys Compd* 2020, **814**: 152240.

[55] Zhu YY. Large electrostrictive properties in lead-free $BaTiO_3$–$ZnSnO_3$ solid solutions. *Appl Phys A-Mater* 2019, **125**: 301.

[56] Fang MX, Ji YC, Zhang Z, *et al.* Re-entrant relaxor–ferroelectric composite showing exceptional electromechanical properties. *NPG Asia Mater* 2018, **10**: 1029–1036.

[57] Pérez R, García JE, Albareda A, *et al.* Motion of 90° and 180° ferroelectric domain wall structures. *Mech Mater* 2010, **42**: 374–382.

[58] Li P, Chen XQ, Wang FF, *et al.* Microscopic insight into electric fatigue resistance and thermally stable piezoelectric properties of (K,Na)NbO_3-based ceramics. *ACS Appl Mater Inter* 2018, **10**: 28772–28779.

[59] Luo NN, Zhang SJ, Li Q, *et al.* PMN-PT based quaternary piezoceramics with enhanced piezoelectricity and temperature stability. *Appl Phys Lett* 2014, **104**: 182911.

[60] Zhang HB, Xu PW, Patterson E, *et al.* Preparation and enhanced electrical properties of grain-oriented ($Bi_{1/2}Na_{1/2}$)TiO_3-based lead-free incipient piezoceramics. *J Eur Ceram Soc* 2015, **35**: 2501–2512.

[61] Acosta M, Novak N, Jo W, *et al.* Relationship between electromechanical properties and phase diagram in the Ba($Zr_{0.2}Ti_{0.8}$) O_{3-x}($Ba_{0.7}Ca_{0.3}$)TiO_3 lead-free piezoceramic. *Acta Mater* 2014, **80**: 48–55.

[62] Narayan B, Malhotra JS, Pandey R, *et al.* Electrostrain in excess of 1% in polycrystalline piezoelectrics. *Nat Mater* 2018, **17**: 427–431.

[63] Davis M, Budimir M, Damjanovic D, *et al.* Rotator and extender ferroelectrics: Importance of the shear coefficient to the piezoelectric properties of domain-engineered crystals and ceramics. *J Appl Phys* 2007, **101**: 054112.

[64] Chen JG, Jin GX, Wang CM, *et al.* Reduced dielectric loss and strain hysteresis in Fe and Mn comodified high-temperature $BiScO_3$–$PbTiO_3$ ceramics. *J Am Ceram Soc* 2014, **97**: 3890–3896.

[65] Arlt G. Twinning in ferroelectric and ferroelastic ceramics: Stress relief. *J Mater Sci* 1990, **25**: 2655–2666.

[66] Maurya D, Zhou Y, Wang YJ, *et al.* Giant strain with ultra-low hysteresis and high temperature stability in grain oriented lead-free $K_{0.5}Bi_{0.5}TiO_3$–$BaTiO_3$–$Na_{0.5}Bi_{0.5}TiO_3$ piezoelectric materials. *Sci Rep-UK* 2015, **5**: 8595.

[67] Liu YX, Li Z, Thong HC, *et al.* Grain size effect on piezoelectric performance in perovskite-based piezoceramics. *Acta Phys Sin-Ch Ed* 2020, **69**: 217704.

[68] Cao WW, Randall CA. Grain size and domain size relations in bulk ceramic ferroelectric materials. *J Phys Chem Solids* 1996, **57**: 1499–1505.